Pore-level Influence of Contact Angle on Fluid Displacements In Porous Media

H.A. Akhlaghi Amiri*[1]
[1] University of Stavanger (UiS), Department of Petroleum Engineering, 4036 Stavanger, Norway
*Corresponding author: hossein.a.akhlaghi-amiri@uis.no

Abstract: Wettability affects two-phase displacements in porous media by determining the microscopic distribution of fluids in pore spaces. The impact of wettability on transport properties at macro-scales has been widely addressed in literature; however pore-level investigations are still demanded for better understanding of the phenomena related to wettability.
In this paper, COMSOL Multiphysics™ was used to investigate the influence of contact angle on two phase (water and oil) flow in porous medium at micro-scale. Cahn-Hilliard phase field equation was solved by finite element with adaptive mesh refinement in 2D modeling done in the present work.
Fluid distributions, saturations and pore-scale displacement mechanisms were completely different for water wet and oil wet systems. Oil film thinning and rupture, fluids' contact line movement and oil drop detachment were recognized as the main pore-level mechanisms in strongly water wet system. Water finger thinning/splitting and water blob trapping were identified in strongly oil wet medium.

Keywords: wettability, contact angle, oil wet, water wet, saturation.

1. Introduction

Flow instabilities (fingering) of the displacing phase is the major cause for inefficient immiscible displacements in porous media [1,2]. Understanding the morphology of the observations is always challenging. The macroscopic transport of the fluids is predictable provided that the pore-level physics of the phenomena is sufficiently understood. One of the factors which impact the flow regimes in porous media is wettability [3].

Medium wettability affects the displacement by determining the microscopic distribution of fluids in pore-spaces. Anderson [4,5] and Morrow [6] reviewed studies that have addressed the impact of wettability on transport properties at macro-scales. However a deeper understanding of wettability effects demands pore-level investigations which are still limited. As an example, Martys et al. [7] investigated the effect of contact angle on fluid invasion in porous media. They have presented a phase diagram for fluid invasion of porous media as a function of pressure and the contact angle of the invading fluid. The degree of wettability is usually related to contact angle (θ_c), which is a boundary condition in determining the interfacial shape. A grain surface is generally considered water wet if $\theta_c < \pi/2$ and oil wet if $\theta_c > \pi/2$.

This paper addresses two phase flow in 2D uniform porous media simulated using coupled Navier-Stokes and Cahn-Hilliard phase field method (PFM). PFM was selected since it is able to realistically capture phenomena related to viscous and capillary forces with a reasonable computational time, compared to other methods such as level set method [8]. The equation system was solved by COMSOL Multiphysics™ with finite element method. Adaptive interfacial mesh refinement was used to reduce the running time. The developed method was validated using non-isothermal Poiseuille flow through a channel, and the results showed good accuracy compared to analytical solution. It is then used to address pore-scale water-oil displacements for investigating the effect of contact angle on the flow patterns and fluid saturations and pressure.

2. Governing Equations

Cahn-Hilliard convection equation is a time dependent form of the energy minimization concept. It is obtained by approximating interfacial diffusion fluxes as being proportional to chemical potential gradients, enforcing conservation of the field [9]. This equation models creation, evolution and dissolution of the interface:

$$\frac{\partial \phi}{\partial t} + u.\nabla \phi = \nabla .(\gamma \nabla G) \qquad (1)$$

where ϕ is a representative of the concentration fraction of the two components and is called order parameter. It takes distinct constant values in the bulk phases (e.g., -1 and 1) and varies rapidly between the constant values across the interface. γ is the diffusion coefficient called mobility that governs the diffusion-related time scale of the interface and *G* is the chemical potential of the system. Mobility can be expressed as $\gamma = \gamma_c \varepsilon^2$, where γ_c is the characteristic mobility that governs the temporal stability of diffusive transport and ε is a capillary width that scales with the interface thickness. The chemical potential is obtained from total energy equation as $G = \lambda\left[\phi\ (\phi^2 - 1)/\varepsilon^2 - \nabla^2\phi\right]$, where λ is the mixing energy density. Equation (1) implies that the temporal evolution of ϕ depends on convective transport due to the divergence free velocity and diffusive transport due to gradients in the chemical potential [10].

To simulate immiscible two phase flow problems, equation (1) is coupled with the incompressible Navier-Stokes and continuity equations with surface tension and variable physical properties as follow:

$$\rho \frac{\partial u}{\partial t} + \rho\, u.\nabla u = -\nabla p + \nabla.\left[\mu(\nabla u + \nabla u^T)\right] + F_{st} \quad (2)$$

$$\nabla.u = 0 \quad (3)$$

where *p* is pressure, ρ is density, μ is viscosity and F_{st} is the surface tension body force. The viscosity and density are defined as functions of order parameter, hence

$$\mu = (\mu_2 - \mu_1) \times (1 + \phi)/2 + \mu_1 \quad (4)$$

$$\rho = (\rho_2 - \rho_1) \times (1 + \phi)/2 + \rho_1 \quad (5)$$

where subscript 1 and 2 denote different phases. Surface body force is calculated by derivation of the total free energy due to the spatial coordinate which is obtained as follows [11]:

$$F_{st} = G\nabla\phi \quad (6)$$

PFM considers surface tension as an intrinsic property corresponding to the excess free energy density of the interfacial region [12]. Surface tension coefficient for PFM is equal to the integral of the free energy density across the interface, which is $\sigma = 2\sqrt{2}\lambda/(3\varepsilon)$ in the case of a planar interface.

3. Model Description and Numerical Schemes

The governing equations are supplemented by standard boundary conditions (e.g., inlet, outlet, no-slip, wetted wall and symmetry), which are specified for each model in the related sections. The details about the boundary equations can be found in the works done by [11, 13]. On the solid wetted grains, the following boundary conditions are used:

$$u = 0 \quad (7)$$

$$n.\varepsilon^2\nabla\phi = \varepsilon^2 \cos(\theta_c)|\nabla\phi| \quad (8)$$

$$n.\frac{\gamma\lambda}{\varepsilon^2}\Delta\psi = 0 \quad (9)$$

where *n* is the unit normal to the wall, θ_c is the contact angle and an auxiliary parameter to decompose fourth-order Cahn-Hilliard equation (1) into two second-order equations. Triangular mesh elements are used in all the computations in this work. Time steps sizes are controlled by the numerical solver during the computations, using backward differentiation formula (BDF).
To avoid numerical distortions, the interface must be thin enough to approximate a sharp interface. A sharp transition minimizes smearing of physical properties as well as better conservation of the area bounded by the zero contour. The interface layer, however, must be resolved by fine mesh. These conditions are described in detail by [13] as model convergence and mesh convergence, respectively. Mobility (γ) is another important parameter that affects the accuracy of the PFM [14]. γ has to be large enough to retain a more or less constant interfacial thickness and small enough to keep the convective motion [11]. Different sensitivity studies have been reported by Akhlaghi Amiri and Hamouda [8] on model convergence, mesh convergence and mobility in modeling two phase flow through porous media using PFM. Considering the average grain diameter in porous medium as the characteristic length (l_c) and

defining Cahn number as $Cn = \varepsilon / l_c$, it was demonstrated that at *Cn*=0.03 and mesh size $h = 0.8\varepsilon$, the model convergence and mesh convergence are satisfied for the phase field method. Simulations with $\gamma_c = 1$ showed less volume shrinkage and more physically realistic results [8].

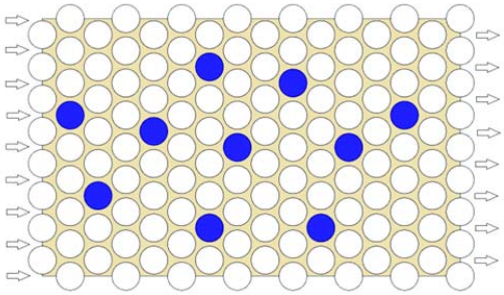

Figure 1. Schematic of the simulated porous medium. The marked blue circles are the enlarged grains by 10%. The position of inlets and outlets are specified with inward and outward arrows, respectively.

A uniform medium with the dimension of $0.015 \times 0.009\ m^2$ is simulated, in which the grains are represented by equilateral triangular array of circles (Figure 1). The bulk grain diameter and pore throat diameter are set as 0.001 *m* and 0.00015 *m*, respectively. To accelerate the formation of fingers, the homogeneity of the medium was slightly disturbed by enlarging the diameter of ten randomly distributed grains by 10% in the medium, as marked in Figure 1. The void fraction (porosity) of the medium is approximately 35%. The grain surfaces are defined as wetted walls having a certain contact angle (θ_c). Oil in place in the medium is displaced by water, injected through inlets on the left hand side of the medium with symmetry boundary conditions on the lateral sides. Water is injected with constant velocity (u_{inj}). In all the numerical experiments in this work, Re is small enough to mimic the laminar regime. According to the reported empirical and numerical works, Re of a laminar flow in porous media ranges between 1 and 10 [15]. The pressure is assumed to be zero at the outlets on the right hand side of the medium. Water and oil densities are set to $\rho = 1000\ kg/m^3$. By considering subscripts *o* and *w* for oil and water, respectively, capillary number is defined as $Ca = \mu_w u_{inj} / \sigma$. *Ca* and viscosity ratio ($M = \mu_w / \mu_o$) quantify fluid characteristics and determine the types of flow instabilities in absence of gravity forces.

4. Results and Discussion

The influence of contact angle is addressed for water-oil displacements at log *Ca*=-3.9 and log *M*=-1.7.

Figure 2 shows the fluid distributions after the displacement was stabilized for different θ_c values of $\pi/4$, $\pi/2$, and $3\pi/4$ corresponding to water wet, intermediate wet and oil wet conditions, respectively. Fingering of the injected water is the common phenomenon in all the simulated cases. However, the water fingers become thinner as the medium becomes less water wet, as shown in Figure 2. When the medium is water wet, Figure 2a, the water phase propagates with three continuous thick fingers with average thickness of 2-3 pore bodies. Two lateral fingers breakthrough, while the middle one becomes stagnant after water breakthrough time. In the medium with the intermediate wetting condition, $\theta_c = \pi/2$, three water fingers are formed with an average thickness of 1-2 pore bodies, of these the two bottom fingers breakthrough and the one in top becomes stagnant. As shown in Figure 2c for the oil wet media, water is split into numerous thin water fingers with average thickness less than a pore body. At $\theta_c = 3\pi/4$, it is observed that two volumes of water with the size of 2-3 pore bodies are trapped in lower part of the medium.

Martys et al. [7] have reported similar observations as they modelled a stepwise quasi-static invasion at different contact angles, using a sequence of circular arcs connecting pairs of disks. They identified three types of instability during all the invasion processes: burst, touch and overlap. They realized that as θ_c decreases, the dominant instability changes from bursts to overlap, in which the interface is smooth and the invading fluid motion is cooperative, in agreement with our observation in Figure 2a, for water wet conditions. Martys et al. [7] have reported that the cooperative overlap mechanism became increasingly important as the invading

fluid became more wetting. On the other hand, they observed that at large θ_c, each throat between pores is invaded independently, leading to fractal patterns (as realized in Figure 2c, in the case of oil wet conditions).

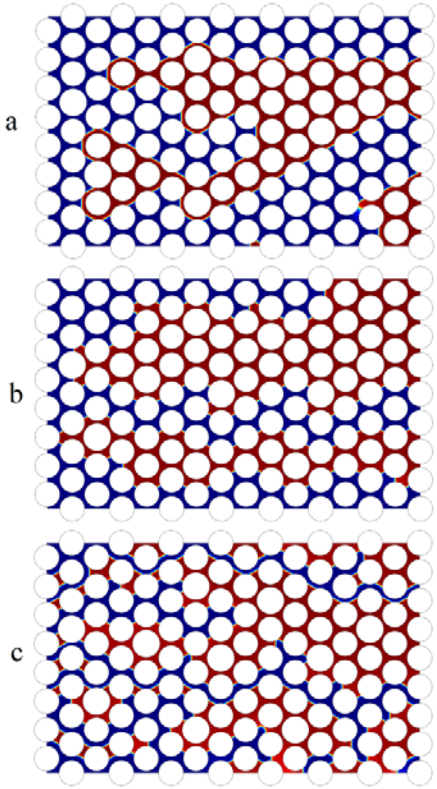

Figure 2. Snapshots of fluid distributions at water breakthrough times for the simulated model with different grain contact angles of a) $\theta_c = \pi/4$, b) $\pi/2$, and c) $3\pi/4$.

Stabilized s_w and average inlet pressure versus s_w for the different tested wetting conditions are plotted in Figure 3. As shown in Figure 3a, higher water saturations are obtained when the medium is more water wet. Water saturation is below 0.5 when medium is oil wet, while it increases more than 30% as the medium becomes strongly water wet. It is worth mentioning, in general, as the medium becomes less water wet, the water breakthrough happens at an earlier time.

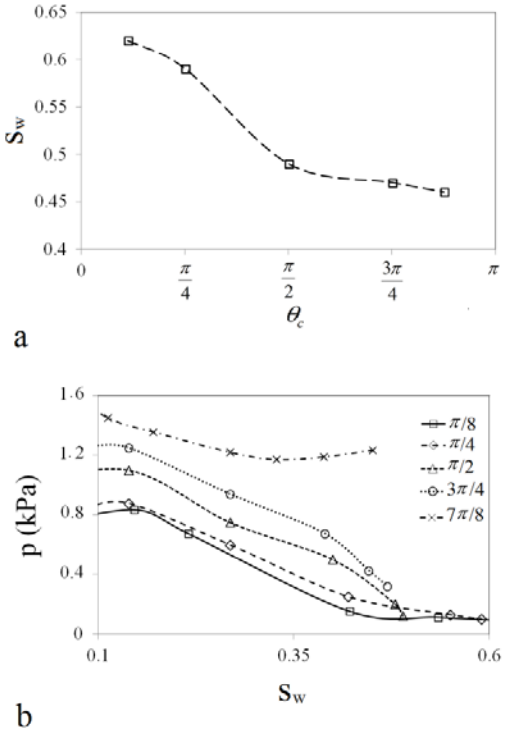

Figure 3. Illustrates the effect of contact angle (θ_c) on (a) water saturation (s_w) at breakthrough time and (b) injection pressure (p) as a function of s_w in the simulated model.

The injection pressure variations during water flooding for different wettability conditions are shown in Figure 3b. For all values of contact angle, except for $\theta_c = 7\pi/8$, the declining pressure trends as a function of s_w are almost the same, however higher pressure trends correspond to a less water wet situation. The high pressures are related to the capillary resistance in the medium, which is called threshold pressure. Threshold pressure is defined here as the minimum pressure necessary for water to enter the pore and throat spaces. Martys et al. [7] also observed that for each θ_c there is a critical pressure (threshold pressure) at which interfaces first span an infinite system. This critical pressure increased as θ_c increased, in agreement with the results presented in Figure 3b.

Different pore-scale mechanisms are observed in water wet and oil wet conditions which affect the efficiency of the displacements.

Figure 4 demonstrates four instants in enlarged sections of the medium during water invasion in strongly water wet and strongly oil wet conditions.

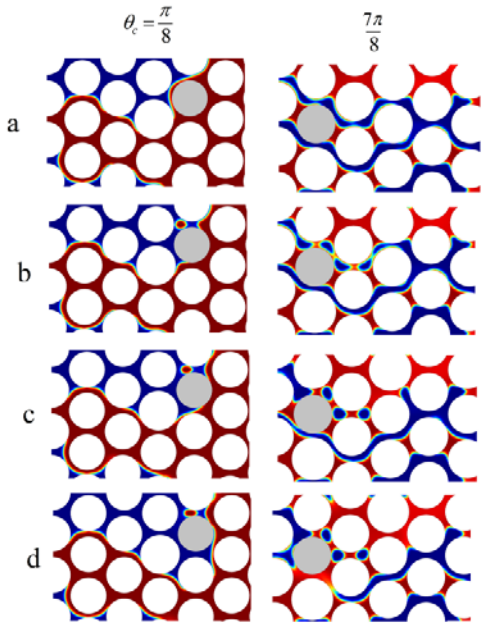

Figure 4. Snapshots of fluid distributions in an enlarged section of the medium at four successive instants of a, b, c and d for strongly water wet ($\theta_c = \pi/8$) and strongly oil wet ($\theta_c = 7\pi/8$) conditions in the simulated model.

In strongly water wet condition ($\theta_c = \pi/8$), three mechanisms of oil film thinning and rupture, water-oil contact line movement and oil drop formation and detachment are observed. These mechanisms have been shown for $\theta_c = \pi/8$ around a gray color marked grain in Figure 4. At instant (a), as water front approaches the marked grain, the film of non-wetting oil phase on the surface of the marked grain narrows until it ruptures; so that the water phase just contacts the grain surface. Upon formation of a water-oil-grain contact line, it moves on the grain surface, instants (b) and (c), until water phase surrounds the grain, instant (d). This sequence repeats for all the water invaded grains. A similar pore-scale displacement mechanism happens in all the imbibition processes, in which wetting phase imbibes into the porous medium and invades the pore network. Another mechanism in strongly water wet systems is formation of oil blobs as a result of water film bridging in pore throats, instants (a) and (b) above the marked grain. The trapped oil drop is initially attached to the surrounded grain walls in the pore body, instant (b). Due to viscous force of the injected water, the oil drop is detached from the grain walls, instant (c), and gradually progresses toward the outlet, instant (d). This observation also confirms the ability of our simulation method to model displacement of blobs in the medium due to viscous forces, which was not possible in pore network modeling in some reported works [3]. The efficiency of oil displacements in strongly water wet media is high due to the pore-scale mechanisms described above.

In strongly oil wet media, the oil phase is found to be present in three distinctive forms: pools that occupy multiple pore bodies, thin films surrounding the grains and bridges between the pore throats. Two pore-scale displacement mechanisms of water finger thinning and splitting and water blob trapping are identified in strongly oil wet medium. As shown in Figure 4 for $\theta_c = 7\pi/8$, the water finger above the marked grain narrows in the throat channels due to growth of oil films around the grains, instant (a), and splits into several parts due to oil film bridging in pore throats, instant (b). This water finger splitting results in forming three small water drops trapped in pore bodies, instant (c). Another water finger splitting phenomenon happens below the marked grain at instant (d) without forming any water blob. Water splitting and trapping reduce the efficiency of oil displacements in oil wet media.

5. Conclusions

Phase field method was employed to model the influence of contact angle on two-phase displacements at pore scale. The simulated models were able to realistically capture the impact of wettability on the fluid distributions and flow parameters such as pressure and fluid saturations. It was found that fluid distributions, saturations and pore-level displacement mechanisms are totally dependent on the medium wettability. Different pore-level displacement phenomena were observed for water wet and oil wet media.

6. References

1. H.A. Akhlaghi Amiri, A.A. Hamouda, Pore-scale modeling of non-isothermal two phase flow in 2D porous media: Influences of viscosity, capillarity, wettability and heterogeneity. *Int. J. Multiphase Flow*. **61**, 14-27 (2014)
2. M. Ferer, C. Ji, G.S. Bromhal, J. Cook, G. Ahmadi, D.H. Smith, Crossover from capillary fingering to viscous fingering for immiscible unstable flow: experiment and modeling. *Phys. Rev*. E 70, 016303 (2004)
3. R. Lenormand, E. Touboul, C. Zarcone, Numerical models and experiments on immiscible displacement in porous media. *J. Fluid Mech.***189**, 165–187 (1988)
4. W.G. Anderson, Wettability literature survey—part 4: the effects of wettability on capillary pressure. *J. Pet. Tech.* **39**, 1283–1300 (1987a)
5. W.G. Anderson, Wettability literature survey—part 5: the effects of wettability on relative permeability. *J. Pet. Tech.* **39**, 1453–1468 (1987b)
6. N.R. Morrow, Wettability and its effects on oil recovery. *J. Pet. Tech.* **42**, 1476–1484 (1990)
7. N. Martys, M. Cieplak, M. Robbins, Critical phenomena in fluid invasion of porous media. *Phys. Rev. Lett.* **66** (8), 1058-1061 (1991)
8. H.A. Akhlaghi Amiri, A.A. Hamouda, Evaluation of level set and phase field methods in modeling two phase flow with viscosity contrast through dual-permeability porous medium. *Int. J. Multiphase Flow* **52**, 22-34 (2013)
9. V.E. Badalassi, H.D. Cenicerob, S. Banerjee, Computation of multiphase systems with phase field models, *Journal of Computational Physics*, **190**, 371-397 (2003)
10. A.A. Donaldson, D.M. Kirpalani, A. Macchi, Diffuse interface tracking of immiscible fluids: improving phase continuity through free energy density selection, *International Journal of Multiphase Flow*. **37**, 777-787 (2011)
11. P. Yue, C. Zhou, J.J. Feng, C.F. Ollivier-Gooch, H.H. Hu, Phase-field simulations of interfacial dynamics in viscoelastic fluids using finite elements with adaptive meshing, *Journal of Computational Physics*, **219**, 47–67 (2006)
12. R.S. Qin, H.K. Bhadeshia, Phase field method, *Material Science and Technology*, **26**, 803-811 (2010)
13. C. Zhou, P. Yue, J.J. Feng, C.F. Ollivier-Gooch, H.H. Hu, 3D phase-field simulations of interfacial dynamics in newtonian and viscoelastic fluids, *Journal of Computational Physics*, **229**, 498–511 (2010)
14. D. Jacqmin, Calculation of two-phase Navier-Stokes flows using phase field modeling, *Journal of Computational Physics*, **155**, 96-127 (1999)
15. M. Hassanizadeh, W. Gray, High velocity flow in porous media. *Transp. Porous Med*. **2**, 521-531 (1987)

7. Acknowledgements

Author acknowledges Dong Energy Company, Norway for the financial support of the work.